






Synthesis, structure, and visible-light-driven activity of *o*-YbFeO₃/*h*-YbFeO₃/CeO₂ photocatalysts

Sofia M. Tikhanova^{ab*} , Lev A. Lebedev^a , Svetlana A. Kirillova^c ,
Maria V. Tomkovich^a , Vadim I. Popkov^a 

a: Ioffe Institute, 194021, Saint Petersburg, Russia

b: Saint-Petersburg State Institute of Technology, 190013, Saint Petersburg, Russia

c: Saint Petersburg Electrotechnical University "LETI", 197376, Saint Petersburg, Russia

* Corresponding author: tihanova.sof@gmail.com

This article belongs to the regular issue.

© 2021, The Authors. This article is published in open access form under the terms and conditions of the Creative Commons Attribution (CC BY) license (<http://creativecommons.org/licenses/by/4.0/>).



Abstract

Photo-Fenton-like oxidation of organic substances is one of the key advanced oxidation processes based on the reversible $\text{Fe}^{2+} \leftrightarrow \text{Fe}^{3+}$ transition and the generation of a strong oxidant $\cdot\text{OH}$ in the presence of H_2O_2 and is currently considered as a promising method for the purification of polluted aqueous media. However, the absence of effective and stable photocatalysts of this process, operating under the action of visible light, necessitates the exploratory studies, mainly among iron oxides and ferrites of various compositions and structures. In this work, using the method of solution combustion followed by heat treatment in air the heterojunction nanocomposites based on ytterbium orthoferrite and cerium dioxide of the composition *o*-YbFeO₃/*h*-YbFeO₃/CeO₂ (0–20 mol.%) with high absorption in the visible region and advanced photo-Fenton-like activity were obtained. The nanocomposites were studied by EDS, SEM, XRD, BET, and DRS methods. The photo-Fenton-like activity of the nanocomposites was investigated during the degradation of methyl violet under the action of visible ($\lambda_{\text{max}} = 410 \text{ nm}$) radiation. As a result, the formation of I-type heterojunction based on stable rhombic (55.4–79.0 nm) and metastable hexagonal (19.5–24.0 nm) modifications of ytterbium orthoferrite (*o*-YbFeO₃ and *h*-YbFeO₃, respectively) and cubic cerium dioxide CeO₂ (13.2–19.2 nm) nanocrystals was established. It was shown that the obtained nanocomposites had foamy morphology and were characterized by a specific surface in the range of 9.1–25.0 m²/g, depending on the CeO₂ content. It was found that nanocrystalline components were chemically and phase-pure, uniformly spatially distributed over the nanocomposite, and had multiple contacts with each other. Based on this fact and the established electronic structure of the nanocomposite components, the formation of I-type heterojunction with the participation of *o*-YbFeO₃ ($E_g = 2.15 \text{ eV}$), *h*-YbFeO₃ ($E_g = 2.08 \text{ eV}$), and CeO₂ ($E_g = 2.38 \text{ eV}$) was shown, the presence of which increased photocatalytic activity of the resulting nanocomposite. The optimal content of CeO₂ in the nanocomposite was 5%, and the *o*-YbFeO₃/*h*-YbFeO₃/CeO₂-5% sample was characterized by the highest rate constant of photo-Fenton-like degradation of methyl violet under the action of visible light equal to $k = 0.138 \text{ min}^{-1}$, which was 2.5 to 5 times higher than for nanocomposites based on ytterbium orthoferrite. The obtained results indicate that the developed nanocomposites can be considered as a promising basis for the advanced oxidation processes for the purification of aqueous media from organic pollutants.

Keywords

ytterbium orthoferrite
cerium dioxide
solution combustion
synthesis
heterojunction
photocatalysts
Fenton-like process

Received: 29.09.2021

Revised: 27.11.2021

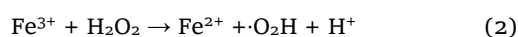
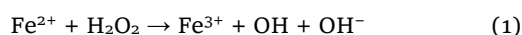
Accepted: 30.11.2021

Available online: 02.12.2021

1. Introduction

Currently, the problem of water purification from organic pollutants is attracting more and more attention. The advanced oxidation processes or AOPs [1] have been actively studied as the basis for promising and effective methods for eliminating pollution from wastewater. These methods are based on the catalytic production and action of hydroxyl radicals (OH·) having the strong oxidizing ability, due to which complex organic molecules can be oxidized partially to simpler molecules or completely to CO₂ and H₂O.

One of the most promising AOPs is the Fenton process, in which Fe²⁺ is used as a catalyst for the formation of hydroxyl radicals, and hydrogen peroxide H₂O₂ is used as their main source [2]. The mechanism of this process can be represented by two main stages following the reaction equations:



The main advantages of this process are its relatively high efficiency and ease of implementation. Since the final products of the decomposition of hydrogen peroxide are oxygen (O₂) and water (H₂O), this process is safe and environmentally friendly, which is important for the purification of aqueous media from organic pollutants [3].

However, the classical homogeneous Fenton process has significant disadvantages, such as high specific cost, limited operating pH range, the formation of a large volume of iron sludge (which has a detrimental effect on the environment and leads to the loss of a large amount of catalytic metals), as well as difficulties in catalyst regeneration (Fe²⁺). To overcome these disadvantages the improved approaches based on the Fenton process are currently being developed and, in particular, a photoinduced Fenton-like heterogeneous process, which eliminates the known limitations. Thus, the development and production of new highly efficient heterogeneous photocatalysts for photoinduced Fenton-like oxidative processes seem to be an urgent task.

Nanostructured ferrites, in particular REE orthoferrites (RFeO₃, where R = Sc, Y, Ln), can be used as the basis for such materials. These compounds have been actively studied due to their practically significant structural [4], magnetic [5–8], electrical [8–10], conducting [11] and photocatalytic properties [12–14]. In particular, ytterbium orthoferrite YbFeO₃ has important for practical applications electrical and magnetic properties that change depending on its crystal structure [15]. Although YbFeO₃ has a thermodynamically stable orthorhombic perovskite structure (*Pbnm/Pnma*), some studies have shown that nanostructured YbFeO₃ (mainly in the form of thin films) can have more two more metastable hexagonal phases: nonpolar *P63/mmc* and polar *P63cm*, depending on the

partial pressure of oxygen [4, 16]. In addition, YbFeO₃ nanoparticles, being in a magnetically ordered state, can be used in catalytic processes [13] and then removed from the reaction solution by applying of an external field, which makes it promising to use them as the basis for effective magnetically controlled photocatalysts for the purification of polluted waters, including using photo-Fenton-like processes.

However, the use of REE orthoferrites in Fenton-like processes is limited by a high tendency to reverse recombination of electron-hole pairs formed during light absorption, as well as by a limited region of radiation absorption (visible region from 500 nm and above). In the previous work, it was shown that the nanocomposite based on *h*-YbFeO₃/*o*-YbFeO₃ exhibits greater photocatalytic activity compared to single-phase *o*-YbFeO₃ at similar specific surface areas. The formation of a heterojunction prevents the recombination of electron-hole pairs and thereby increases the overall photocatalytic efficiency of the nanocomposite material [15, 17], but does not significantly affect the characteristic region of radiation absorption.

To solve this problem, this work proposes the development of nanocomposite photocatalysts based on ytterbium orthoferrite and a co-catalyst, cubic cerium oxide (CeO₂). The use of CeO₂ as a co-catalyst shifts the absorption edge to the ultraviolet region of the spectrum [16], which should lead to an increase in the efficiency of the photocatalytic system in the photo-Fenton-like process due to the more efficient absorption of photons with different energies.

The main methods for obtaining single-phase REE orthoferrites are hydrothermal [4, 18], sol-gel [19] and microwave [20]. However, the preparation of nanocomposites of the above composition presents a certain difficulty, since the chemical properties of the corresponding components differ significantly and such systems cannot always be obtained by known approaches and synthetic methods. In this work, we propose the preparation of the *o*-YbFeO₃/*h*-YbFeO₃/CeO₂ nanocomposite by the method of solution combustion, carried out in a soft glow mode, followed by a heat treatment of amorphous products at moderate temperatures in air.

2. Experimental

Nanocomposites based on ytterbium orthoferrite and cerium dioxide were obtained by solution combustion followed by heat treatment. A schematic representation of the synthesis procedure is shown in Fig. 1. Glycine (C₂H₅NO₂, 98.5%) was added to a solution of oxidizing salts Yb(NO₃)₃·6H₂O (99.5%), Fe(NO₃)₃·9H₂O (98.0%) and Ce(NO₃)₃·6H₂O (99.5%), and ratio *G/N* = 0.2, provided a glowing combustion mode and the formation of amorphous products [21]. Ytterbium, iron, and cerium nitrates were taken in the ratios required to obtain *o*-YbFeO₃/*h*-YbFeO₃/CeO₂ samples with a molar fraction

of cerium dioxide of 0, 2.5, 5, 7.5, 10, and 20%. The reagents were dissolved in 10 ml of distilled water with constant stirring for 15–20 minutes, after which the reaction mixture was heated until almost complete removal of water, transformation into a gel-like mass, and autoignition. A dark brown foamy solid was formed, which was then heat-treated in the air for 24 hours at 800 °C to completely remove organic residues and form crystalline products.

The elemental composition of the synthesized samples was studied using energy-dispersive X-ray spectroscopy (EDS) on a Tescan Vega 3 SBH scanning electron microscope equipped with Oxford INCA X-act X-ray microanalysis. X-ray phase analysis was performed on Rigaku SmartLab 3 powder X-ray diffractometer using Cu K α ($\lambda = 1.540598 \text{ \AA}$). Powder X-ray diffraction data were obtained with a step of 0.01° and a rate of $4.5^\circ/\text{s}$ in the 2θ range from 20° to 60° . Qualitative X-ray phase analysis was performed using the ICSD powder diffraction database. The average crystallite size was calculated from the broadening of X-ray diffraction lines using the method of fundamental parameters, implemented in the

SmartLab Studio II software package. Quantitative X-ray phase analysis was carried out using the Rietveld method and structural data of crystalline phases. Diffuse reflectance spectra in the UV-visible region (DRS) were measured using an Avaspec-ULS2048 spectrometer equipped with an AvaSphere-30-Refl integrating sphere.

The photocatalytic activity of the obtained catalysts was studied using the example of the photodegradation of methyl violet (MV) in the presence of hydrogen peroxide H_2O_2 . The process was carried out in a transparent glass beaker, under a light source $\lambda_{\text{max}} = 410 \text{ nm}$ with constant stirring. In the course of the experiment, 1.5 mg of the catalyst were suspended in 1 ml of distilled water and added to 1 ml of MV solution (3 mmol/L), after which 10 ml of an H_2O_2 solution with a concentration of 20 mmol/L were added to start the reaction. In photocatalytic experiments, the concentration of the dye was determined spectrophotometrically. AvaLight-XE light source and Avaspec-ULS2048 spectrometer were used to measure the absorption spectra. Decolorization MV measurements were taken every 10 minutes.

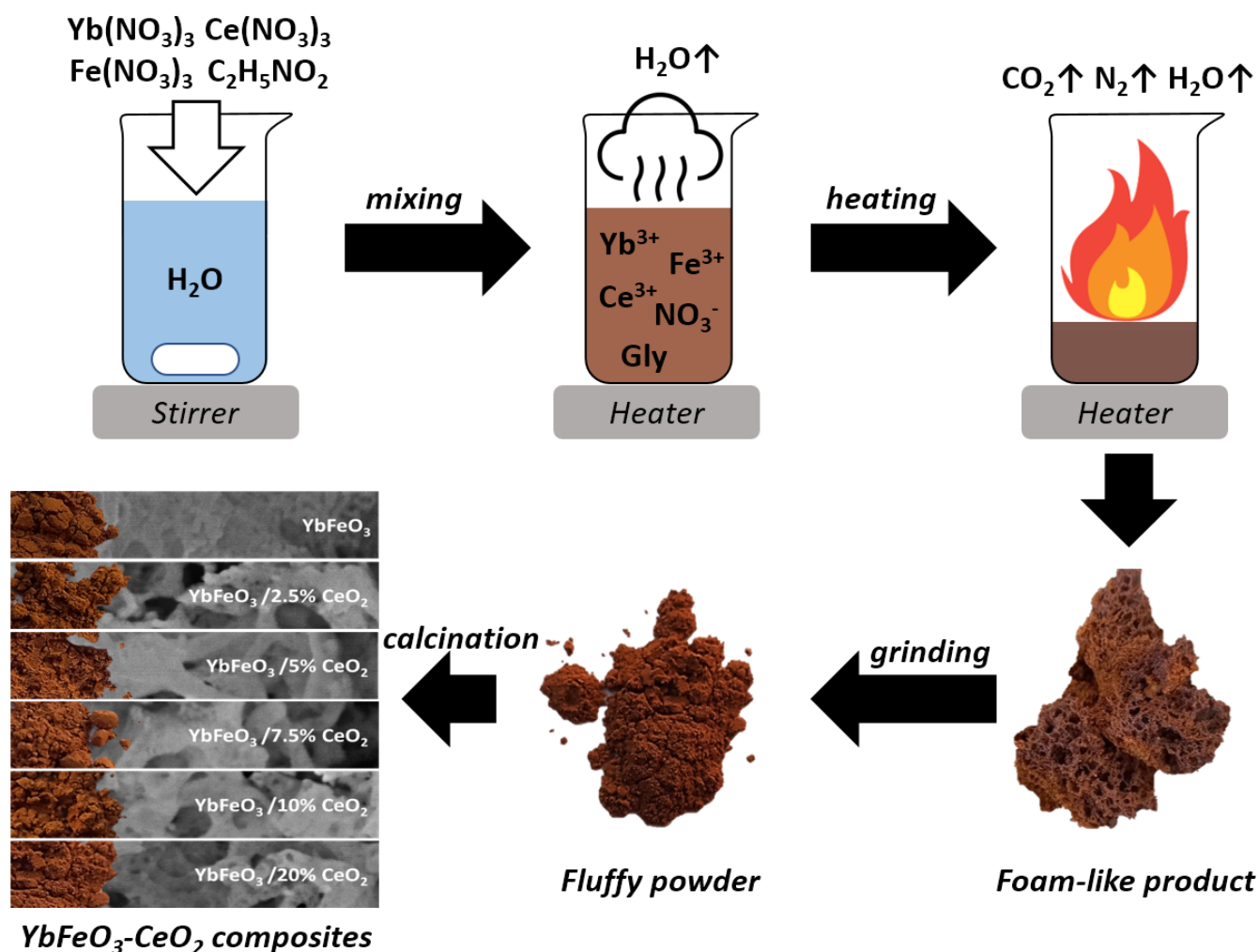


Fig. 1 Procedure for the preparation of $o\text{-YbFeO}_3/h\text{-YbFeO}_3/\text{CeO}_2$ nanocomposite

3. Results and discussion

According to the results of the EDS analysis, in the samples obtained by the method described above, in the general case, the presence of four main elements is observed – ytterbium (Yb), cerium (Ce), iron (Fe), and oxygen (O) (Fig. 2a). No impurity elements were found, which indicates a high chemical purity of the obtained compositions. The result of the quantitative analysis of a series of samples is presented in Fig. 2b. The error of the determination method for heavy elements is about 0.5 wt.%, it was stated that the compositions of the composites for the main

elements (Yb, Ce, Fe) were in good agreement with the composition specified during their synthesis. The stoichiometric relationship is also confirmed by X-ray diffraction data since no reflections of ytterbium oxide or any of the iron oxides are observed. These facts confirm the successful synthesis of samples with a molar content of cerium of 0, 2.5, 5, 7.5, 10, and 20%.

To determine the uniformity of distribution of key chemical elements over the volume of α -YbFeO₃/*h*-YbFeO₃/CeO₂-5% composition, SEM study, combined with EDS mapping, was carried out; its results are presented in Fig. 3.

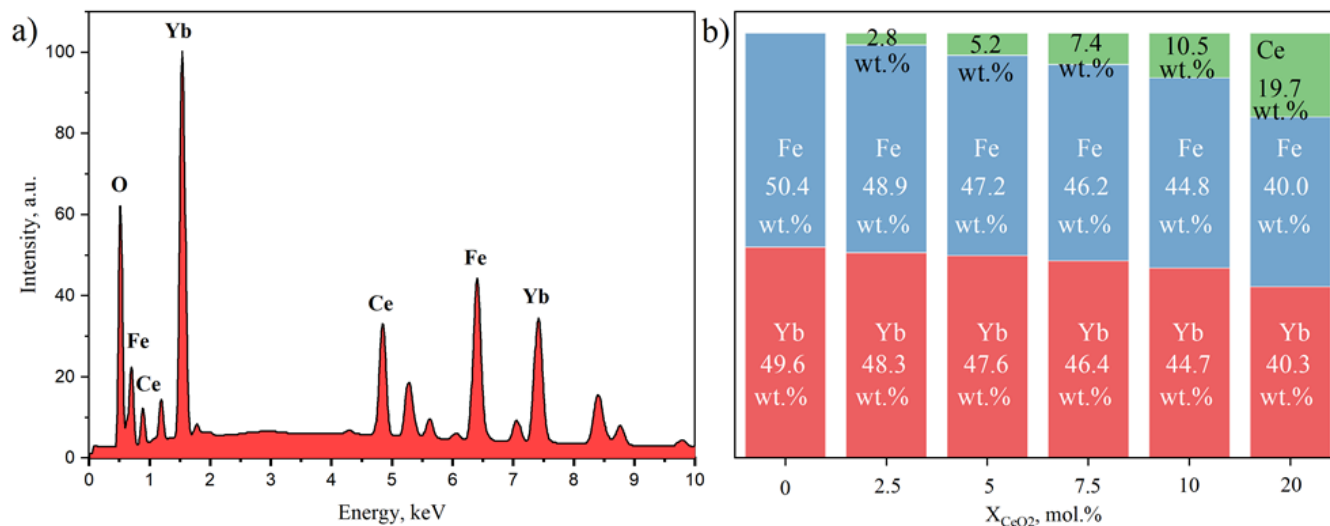


Fig. 2 Typical EDS spectrum of the α -YbFeO₃/*h*-YbFeO₃/CeO₂-5% nanocomposite (a) and the composition of the obtained samples concerning the main elements (in wt.%) (b)

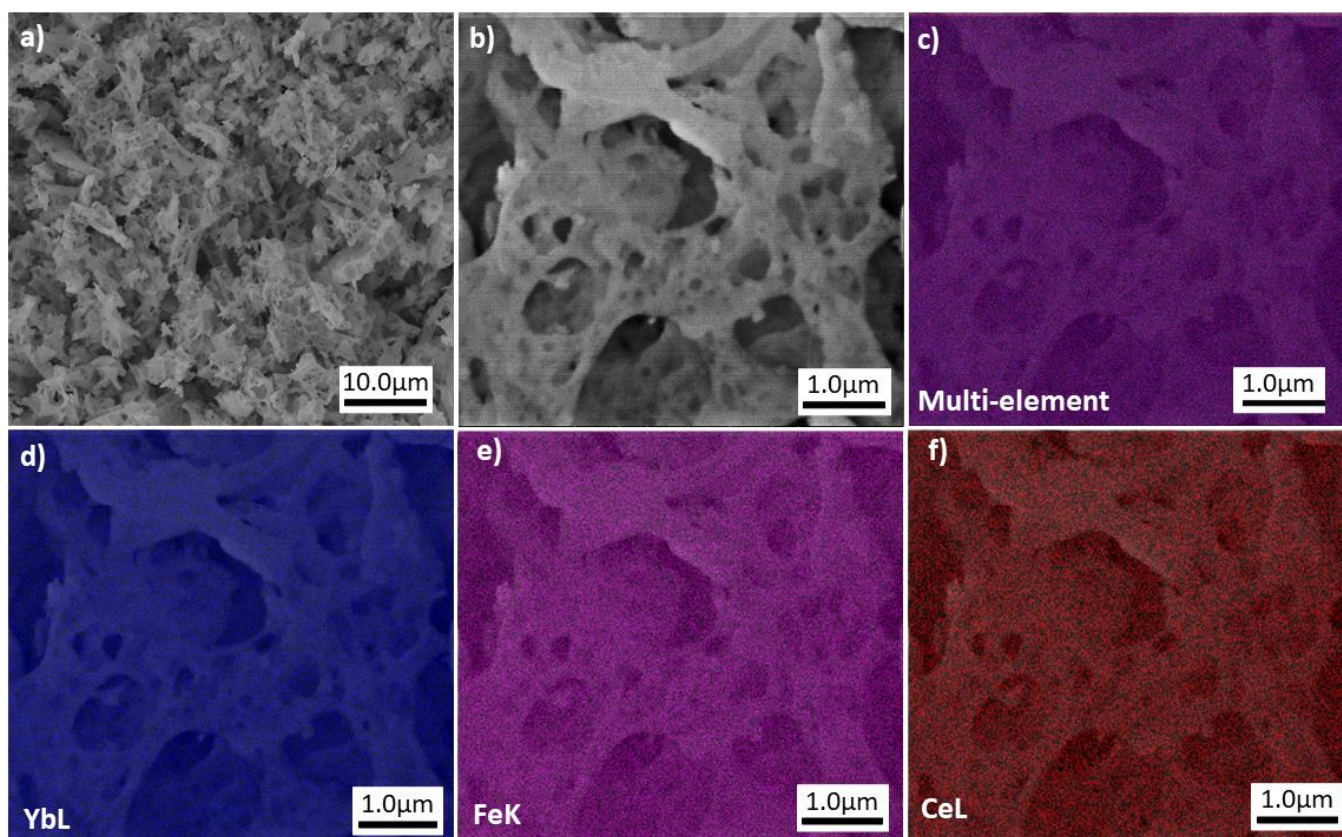


Fig. 3 SEM images (a, b), multi-element (c) and single-element (d-f) EDS mappings of the α -YbFeO₃/*h*-YbFeO₃/CeO₂-5% sample

The area selected based on the SEM results for mapping (Fig. 3a, b) reflects the typical foam-like morphology of powders – products of solution combustion. At the same time, a comparison of the results of multi-element and single-element mapping indicates a high uniformity of the distribution of all the main elements – Yb, Ce, and Fe. No areas with enrichment in one of the elements were found in the results of the EDS mapping. This also indirectly confirms the presence of a large number of contacts between Yb, Ce, and Fe-containing phases in the composition of the obtained composites.

Fig. 4a shows the diffraction patterns of the samples with different CeO₂ contents subjected to heat treatment at 800 °C for 24 hours. According to the qualitative X-ray phase analysis, the YbFeO₃ sample, which does not contain cerium oxide, is a single-phase orthorhombic *o*-YbFeO₃. The samples composed of CeO₂ contain two phases of ytterbium orthoferrite – metastable hexagonal *h*-YbFeO₃ and stable orthorhombic *o*-YbFeO₃. As the mole fraction of CeO₂ increases, a broadening and an increase in the intensity of the peaks corresponding to cerium oxide are observed, while the relative intensity of the peaks corresponding to *o*-YbFeO₃ does not change. It is known that cerium is capable of forming perovskite-like compounds of the *o*-CeFeO₃ type [22]; however, due to the relatively

large ionic radius of Ce³⁺ and its low stability in the air, such compounds are oxidized at elevated temperatures with decomposition to more stable CeO₂ and iron oxides. For this reason, the cerium orthoferrite phase was not detected in the composition of the samples, and the presence of cerium was observed exclusively in the form of cerium (IV) dioxide. In addition, for the samples containing CeO₂, the formation of the *h*-YbFeO₃ phase is observed, which was not previously seen in this system under similar conditions without the addition of cerium [23]. The formation of the hexagonal phase of ytterbium orthoferrite in this case can be caused by the influence of the formed cerium (IV) dioxide, which creates spatial restrictions during crystallization and restricts mass transfer. The combination of these factors creates the conditions for the formation of metastable *h*-YbFeO₃, which, like the hexagonal orthoferrites of other REEs, are stable only for small nanocrystals (usually less than 15 nm) [24].

The concentration dependencies in Fig. 4b were obtained with the Rietveld method by using Rigaku SmartLab Studio II software. The parameters of refinement and criteria of obtained refinement are presented in Fig. 5 and Table 1. The *R*_{wp}, *R*_p, and *R*_e parameters show that the calculated XRD pattern is in good correspondence with measured data.

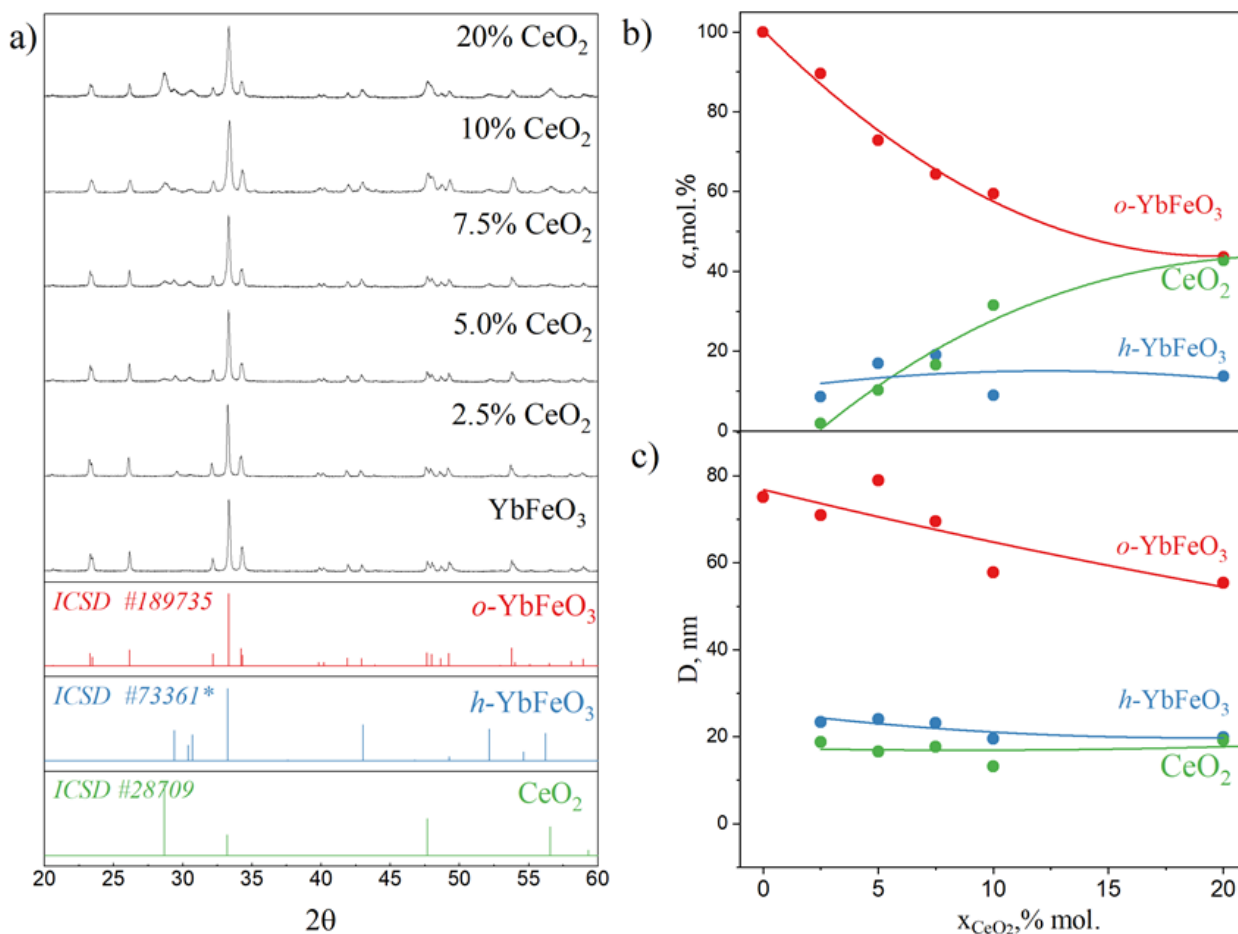


Fig. 4 X-ray diffraction results of *o*-YbFeO₃/*h*-YbFeO₃/CeO₂ (a), molar fraction (mol.%) (b) and average crystallite sizes (c) versus CeO₂ content (mol.%)

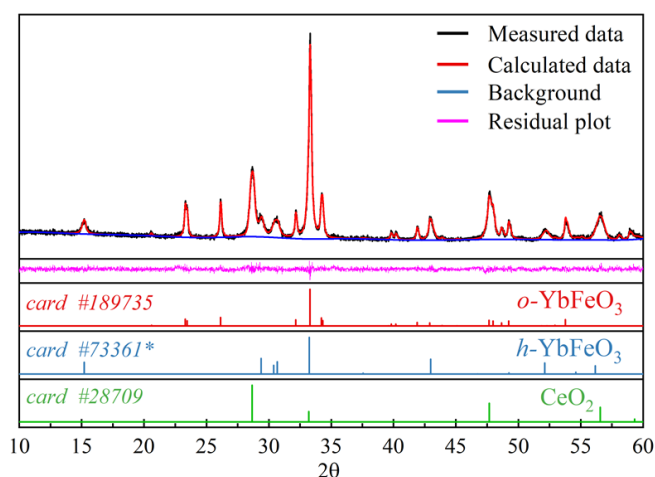


Fig. 5 Rietveld refinement result for the X-ray diffraction of *o*-YbFeO₃/*h*-YbFeO₃/CeO₂

Table 1 The parameters of refinement by the Rietveld method and criteria of obtained refinement

Parameters	<i>o</i> -YbFeO ₃	<i>h</i> -YbFeO ₃	CeO ₂
Initial CIF	ICSD#189735	isostructural to ICSD#73361	ICSD#20194
Crystal system	Orthorhombic	Hexagonal	Cubic
Space group	62: <i>Pbnm</i>	194: <i>P63/mmc</i>	225: <i>Fm$\bar{3}m$</i>
Fraction, mol.%	43.58	13.67	42.75
Average crystal size, nm	47.2	27.8	25.0
<i>a</i> , Å	5.2395	3.50703	5.39149
<i>b</i> , Å	5.5628	3.50703	5.39149
<i>c</i> , Å	7.5788	11.65325	5.39149
α , °	90	90	90
β , °	90	90	90
γ , °	90	120	90
<i>R</i> _w p, %	4.26	4.25	4.25
<i>R</i> _p , %	3.35	3.35	3.35
<i>R</i> _e , %	4.31	4.31	4.31
<i>S</i>	0.9867	0.9853	0.9854

The change in the degree of conversion for crystalline phases, calculated from the data of X-ray diffraction, is presented in Fig. 4b. With an increase in the cerium content in the composite, the molar fraction of *o*-YbFeO₃ steadily decreases, while the molar fraction of CeO₂ increases. In addition, in the presence of cerium in the composition, the appearance of the *h*-YbFeO₃ phase is observed, the fraction of which remains practically the same with a change in the cerium content. In addition to the change in the molar fraction of crystalline phases the gradual broadening of the diffraction peaks also occurs, based on which it is possible to estimate the change in the average size of the corresponding crystallites depending on the cerium content (Fig. 4c). It was found that the crystallite sizes varied in the range 55.4–79.0 nm for *o*-YbFeO₃, 19.5–24.0 nm, and 13.2–19.2 nm for *h*-YbFeO₃ and

CeO₂, respectively. The absence of a noticeable change in the average crystallite size of the *h*-YbFeO₃ and CeO₂ phases is explained by their relatively small fractions in the composition of the composites, which does not allow them to increase their size due to recrystallization processes – the dominant *o*-YbFeO₃ phase prevents such mass transfer. Earlier, using a similar system as an example, it has been demonstrated that for the structural transition hexagonal → orthorhombic REE orthoferrite nanocrystals of the hexagonal phase should reach the critical size [25]. Therefore, due to the limited mass transfer, *h*-YbFeO₃ nanocrystals do not acquire the critical size and remain in a metastable state. Such mutual influence of the components in the *o*-YbFeO₃/*h*-YbFeO₃/CeO₂ system suggests the presence of multiple contacts of individual phases and confirms the heterojunction structure of the resulting composite.

The results of scanning electron microscopy (Fig. 6) indicate that the obtained samples have a highly porous, foamy structure, which is a consequence of the used synthetic method used, characterized by the violent release of gaseous reaction products and foaming of solid-phase products [23]. In this case, even after heat treatment, the foamy morphology is retained at the microlevel, while at the level of individual nanoparticles there are visible morphological changes. Thus, in the case of pure YbFeO₃ without added cerium (Fig. 6a), the distinguishable nanoparticles are weakly agglomerated, have a spherical morphology, and are aggregated into foam-like structures of micron sizes. As shown earlier, the products of solution combustion have foam-like morphology and orthoferrite nanocrystals are formed upon heat treatment of the initial amorphous product from the pore walls while maintaining the foam microstructure [24]. Alternatively, in the case of samples obtained with the addition of cerium (Fig. 6b–f), there is a more monolithic aggregation of individual particles, which are less distinguishable. This may point to the presence of more finely dispersed *h*-YbFeO₃ and CeO₂ phases in the space between the main coarse-crystalline *o*-YbFeO₃ phase. It is worth noting that the size of *o*-YbFeO₃ nanoparticles regularly decreases with the addition of cerium, which is also confirmed by the XRD results (Fig. 4c).

The results of determining the specific surface area of the samples by the BET method are presented in Fig. 7. According to these data, when cerium is added to the system based on YbFeO₃ up to a content of 5.0 mol.%, a 2.5-fold increase in the specific surface area is observed. However, with a further increase in the cerium content, this escalation is replaced by a reduction, and at 20 mol.% cerium, the specific surface area becomes almost the same as that of the pure YbFeO₃ sample. The observed pattern is in good agreement with the results of scanning electron microscopy (Fig. 6) and the increase in the specific surface area in the first range is explained by the appearance of *h*-YbFeO₃ and CeO₂ nanocrystals with a larger specific surface area than *o*-YbFeO₃ due to smaller crystallite sizes.

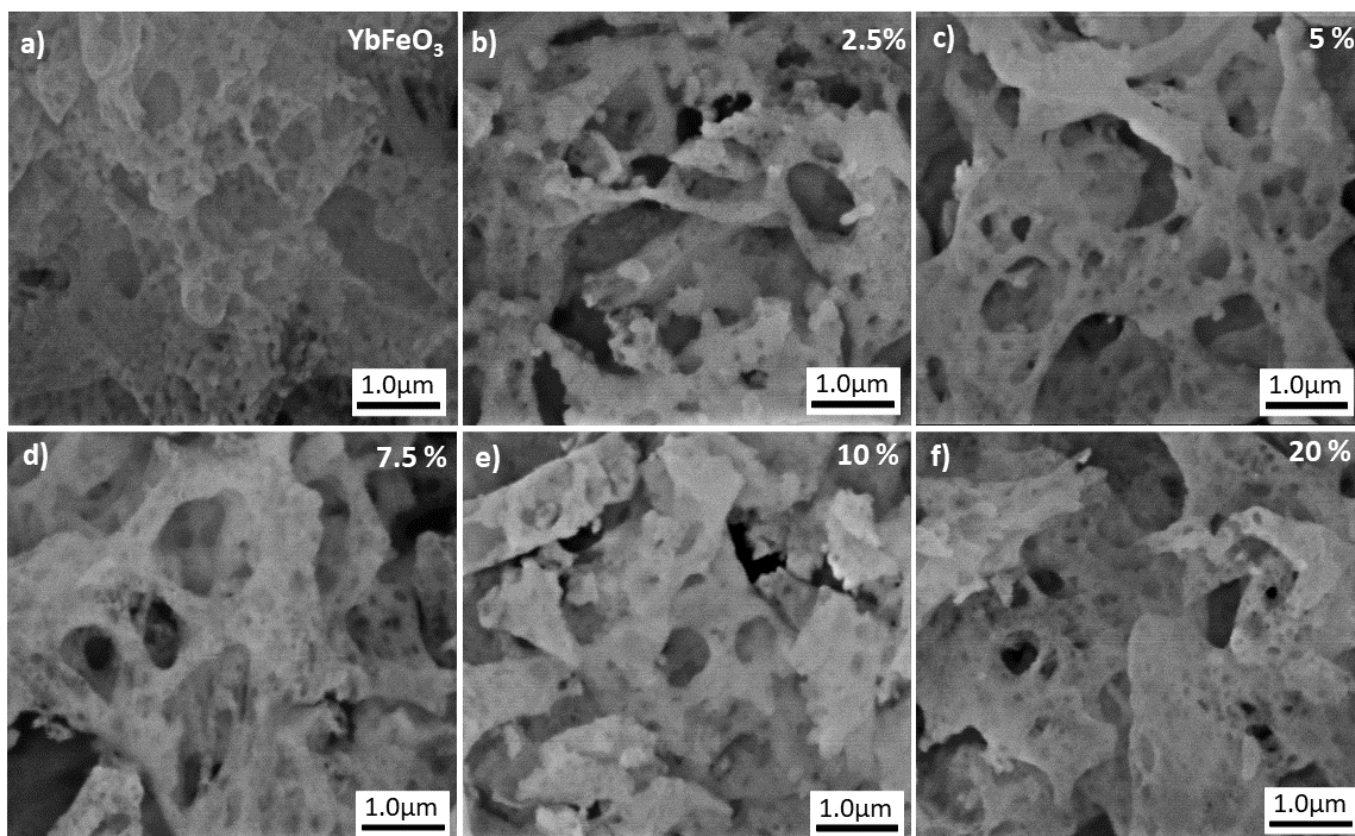


Fig. 6 SEM images of o -YbFeO₃/ h -YbFeO₃/CeO₂ samples with different cerium content: 0% (a), 2.5% (b), 5% (c), 7.5% (d), 10% (e) and 20% (f)

The decrease in the specific surface area in the second composition range is associated with the intensification of aggregation processes due to the increased cerium content, as a result of which the part of the nanocrystal surface is inaccessible for contact. Thus, the o -YbFeO₃/ h -YbFeO₃/CeO₂ sample has the largest specific surface area and it is 25.0 m²/g, which is noticeably higher than for samples based on pure o -YbFeO₃ and o -YbFeO₃/ h -YbFeO₃ composite [23].

The diffuse reflectance spectra of the obtained samples (Fig. 8a) reveal that they intensively absorb the radiation of the visible spectrum. Several inflections in these dependences confirm the presence of several phases with different optical absorption edges in the samples. To determine the band gap of these phases, the experimental data were recalculated into the Tauc coordinates (Fig. 8b), and the calculation results for o -YbFeO₃, h -YbFeO₃, and CeO₂ are shown in Fig. 8c. According to the calculations, the band gaps for all phases do not depend on the cerium content in the samples, as evidenced by their non-systematic variation within the error of the determination method. The average values of the band gaps were 2.15 eV for o -YbFeO₃, 2.08 eV for h -YbFeO₃, and 2.38 eV for CeO₂, which is in good agreement with the literature data [4, 16, 18–20]. Thus, the synthesis of a nanocomposite based on the separate o -YbFeO₃, h -YbFeO₃, and CeO₂ phas-

es with the absence of incorporation of cerium into the structure of ytterbium orthoferrite and ytterbium into the structure of cerium (IV) dioxide is confirmed.

Based on the data on the average values of the band gap, the boundaries of the valence and conduction bands for all phases were determined using the empirical formulas [26]. The transition energies of orthorhombic and hexagonal ytterbium ferrites are close to each other, but their difference affects the electronic structure.

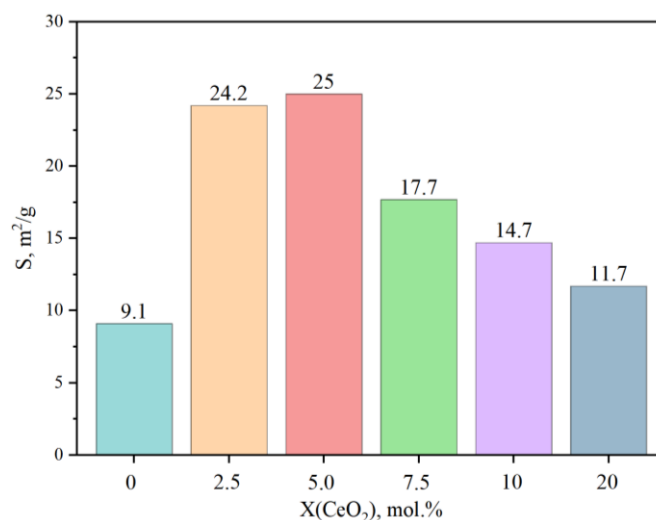


Fig. 7 BET surface area of the o -YbFeO₃/ h -YbFeO₃/CeO₂ samples versus CeO₂ content

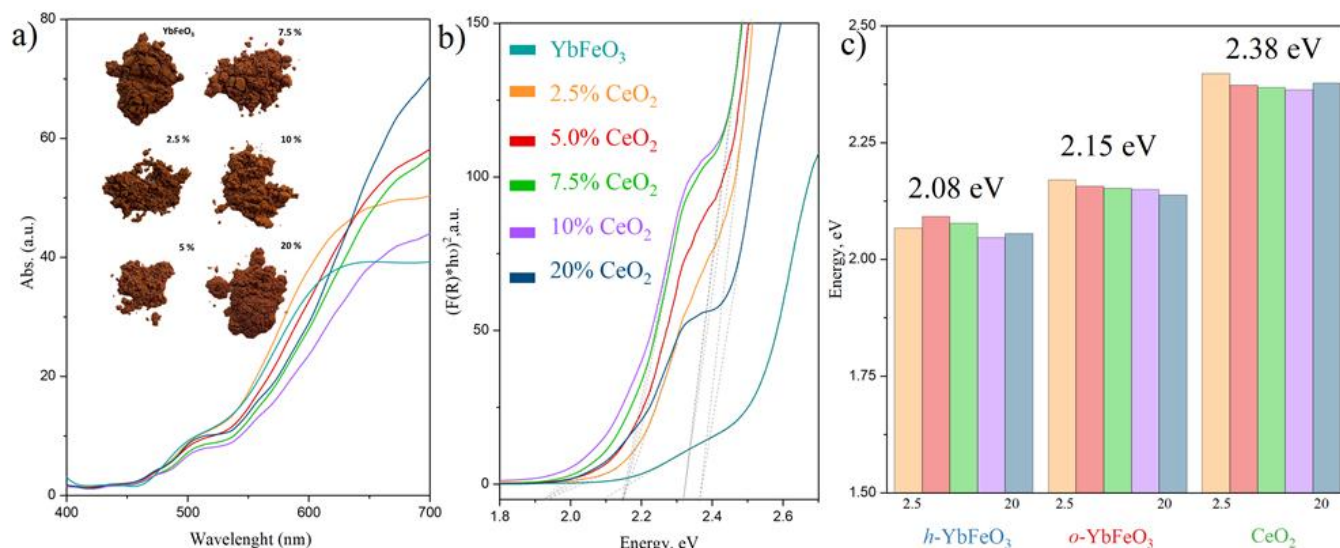


Fig. 8 DRS spectra (a), Tauc plots (b) and band gap energies (c) of the *o*-YbFeO₃/*h*-YbFeO₃/CeO₂ samples

The calculation results are presented in Table 2 and their comparison allows us to conclude that a type I heterojunction structure is formed within the obtained composites, which is suitable for suppressing the processes of reverse recombination of electron-hole pairs in photocatalytic processes.

Table 2 Parameters of the electronic structure of *o*-YbFeO₃/*h*-YbFeO₃/CeO₂ composite

	E_{R1} , eV	χ , eV	E_{CB} , eV	E_{VB} , eV
<i>o</i> -YbFeO ₃	2.15	5.574	0.00	2.15
<i>h</i> -YbFeO ₃	2.08	5.574	0.03	2.11
CeO ₂	2.38	5.56	-0.10	2.28

The photocatalytic activity of the obtained samples was studied in the process of photo-Fenton-like decomposition of methyl violet in the presence of hydrogen peroxide under the action of visible light. Fig. 9a shows the MV spectra of the reaction solution obtained at different times after the start of the photocatalytic experiment. From these data, it follows that in the presence of *o*-YbFeO₃/*h*-YbFeO₃/CeO₂-5% composite, almost complete decolorization of the solution occurs within 90 minutes, which characterizes the composite as an effective catalyst for Fenton-like processes [27].

To assess the effectiveness of the nanocomposites obtained in this work the kinetic studies were carried out, the results of which are presented in Fig. 9b. Before the start of photocatalytic experiments, the reaction solution with the particles of the composite distributed in it was continuously mixed and kept in the dark until the adsorption-desorption equilibrium was established. At the same time, the drop in the concentration of the dye in the solution for the samples differed and correlated with the values of their specific surface area – the higher the specific surface area of the sample, the more MV was adsorbed on its surface (see the initial interval in Fig. 9b). After the equilibrium was established the series of photocatalytic experiments were carried out and the obtained kinetic dependences indicated a differ-

ent methyl violet photodegradation rate in the presence of the obtained nanocomposites and pure ytterbium orthoferrite. By the end of the experiment, the highest photodegradation efficiency was observed for samples with a cerium dioxide molar concentration of 2.5 and 5.0% and amounted to 94.0% and 96.4%, respectively. Thus, the nanocomposites exhibit almost 1.5 times higher efficiency of photodegradation than a sample of pure ytterbium orthoferrite, which is explained by the heterojunction structure of nanocomposites increasing the generation of electron-hole pairs and reducing their recombination. The activity of pure cerium dioxide in this process is very low, which is explained by the absence of photons in the visible radiation spectrum with energy, sufficient for the transition of an electron from the valence band to the conduction band.

For a quantitative comparison of the photocatalytic performance of nanocomposites and pure ytterbium orthoferrite, the obtained kinetic dependences were rearranged into logarithmic coordinates, $-\ln(C/C_0) = f(t)$. The linearization of all kinetic dependences in these coordinates confirms the occurrence of photodegradation of methyl violet accompanied by nanocomposites in the pseudo-first-order characteristic of Fenton-like processes [3]. From the slope of the obtained dependences, the rate constants of the photodegradation reaction were determined. These and the other characteristics of the photocatalysts are summarized in Table 3 and a visual comparison of the obtained reaction rate values is shown in Fig 9d.

According to the results obtained, with an increase in the CeO₂ content, the rate constant values first increase up to 5% CeO₂ and then decrease. The initial trend is associated with promoting charge separation/transfer and reducing overpotential for oxidation, and its change into a downward trend is explained by covering active sites on photocatalyst, shielding the light absorption, decreasing the surface area and activity, increasing the charge recombination.

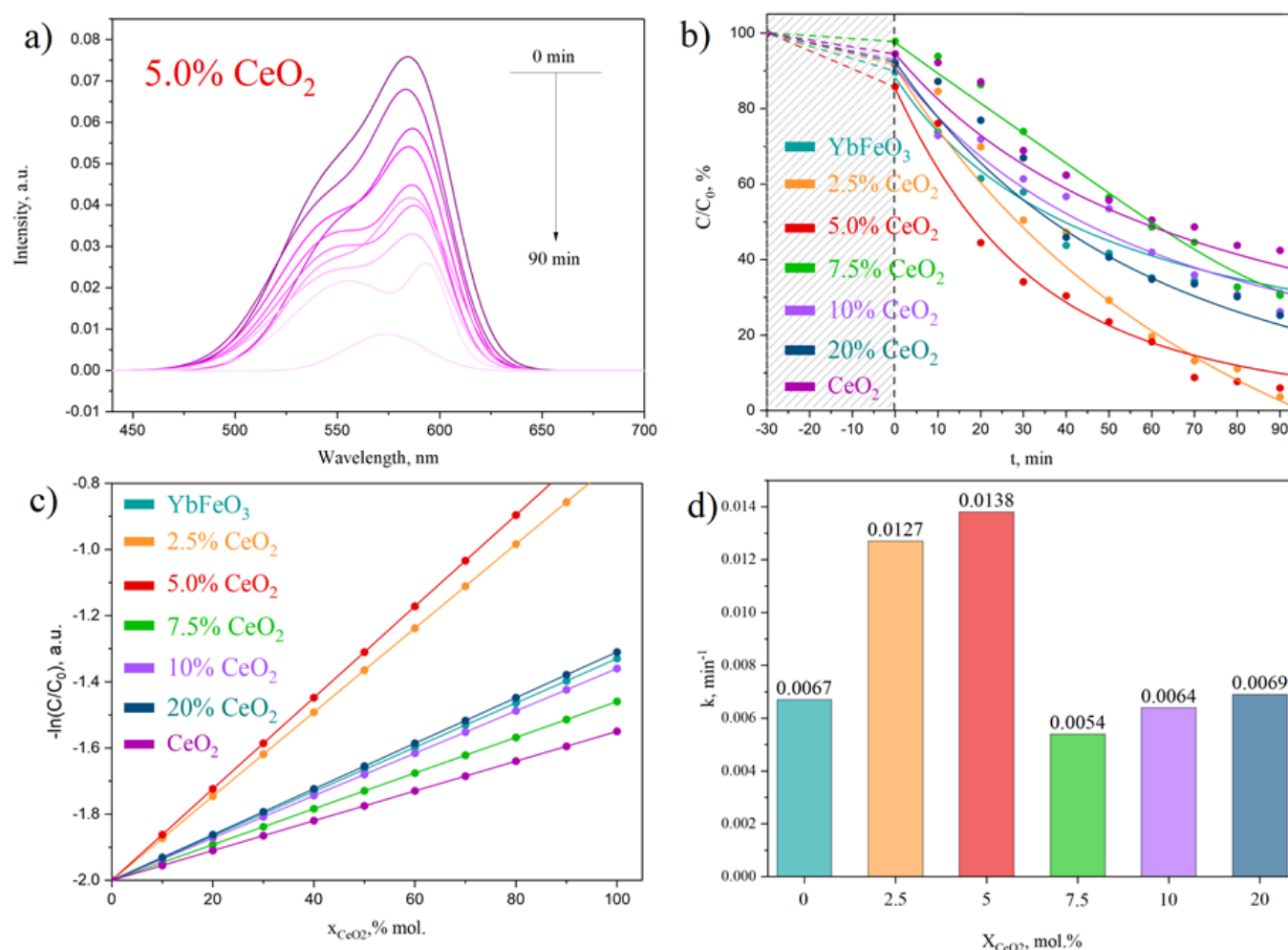


Fig. 9 Photo-Fenton-like degradation of MV over *o*-YbFeO₃/*h*-YbFeO₃/CeO₂-5% catalyst under visible light (a) kinetic curves (b) and logarithmic kinetic curves of the pseudo-first-order process (c) and photodecomposition rate constant (d) versus cerium dioxide content

Table 3 Kinetic parameters of Fenton-like degradation of methyl violet in the presence of photocatalysts based on YbFeO₃ under visible light irradiation

X(CeO ₂), mol.%	Organic compound	Half-life time, min	Degradation efficiency, %	The reaction rate constant, min ⁻¹	R	Ref.
0	MV	35	68.90	0.0067	0.929	This work
2.50	MV	20	96.40	0.0127	0.957	
5	MV	30	94.00	0.0138	0.990	
7.5	MV	60	69.43	0.0054	0.985	
10	MV	45	73.80	0.0064	0.986	
20	MV	40	74.70	0.0069	0.986	
100	MV	65	57.60	0.0045	0.985	
YbFO-700	MV	-	66.20	0.0048	0.991	[23]
YbFO-800	MV	-	47.40	0.0031	0.988	[23]
LaFeO ₃	Acid Orange 7	-	40.70	0.0097	0.952	[28]
LaFeO ₃ /CeO ₂	Acid Orange 7	-	28.40	0.0070	0.971	[28]
BiFeO ₃	BR46	-	95.00	0.0292	0.970	[29]
CoFe ₂ O ₄	BR46	-	44.00	0.0054	0.9663	[30]

Thus, the content of cerium dioxide in the nanocomposite equal to 5% is optimal for the given system and the method of its preparation. The corresponding value of the constant $k = 0.138 \text{ min}^{-1}$ is 2.5–5 times higher than that for the similar systems based on ytterbium orthoferrite (Table 3).

Based on the results of this work, the information obtained on the electronic structure of nanocomposites and their photocatalytic properties, as well as the literature data, a schematic representation of the mechanism of photo-Fenton-like degradation of methyl violet in the pres-

ence of $\text{YbFeO}_3/\text{CeO}_2$ nanocomposite under the action of visible light was proposed (Fig. 10).

Under the action of visible radiation the electron-hole pairs are formed in the components of the composite based on ytterbium orthoferrite, which absorbs in the visible region. Since the energy of the conduction band for CeO_2 is higher than that for $o\text{-YbFeO}_3$ and $h\text{-YbFeO}_3$, and the energy of the valence band, on the contrary, is lower, the resulting nanocomposite has a combination of type I heterojunctions cascaded into each other. This arrangement allows the holes to migrate from CeO_2 to $o\text{-YbFeO}_3$ and from there to $h\text{-YbFeO}_3$, oxidizing OH^- to $\cdot\text{OH}$, which is the strongest oxidizing agent. In addition, electrons can also cascade from CeO_2 to $o\text{-YbFeO}_3$, and then to $h\text{-YbFeO}_3$, initiating the $\text{Fe}^{3+} \rightarrow \text{Fe}^{2+}$ reduction. The presence of H_2O_2 makes it possible for the Fenton-like process to arise. As shown earlier in [23], Fe^{2+} is formed on the surface of $h\text{-YbFeO}_3$ during the reduction of Fe^{3+} by electrons transferred from the $o\text{-YbFeO}_3$ conduction band. During the reaction, Fe^{2+} is oxidized by H_2O_2 to Fe^{3+} and $\cdot\text{OH}$ radicals are formed. Due to the addition of CeO_2 to the system, a similar process can occur on the $o\text{-YbFeO}_3$ surface through electrons supplied from the conduction band of cerium oxide. The interaction of $\cdot\text{OH}$ with methyl violet leads to its oxidation to the most stable products – CO_2 and H_2O . Since the Fenton-like process of the formation of $\cdot\text{OH}$ radicals is activated both on the surface of $h\text{-YbFeO}_3$ and $o\text{-YbFeO}_3$, the heterojunction $h\text{-YbFeO}_3/o\text{-YbFeO}_3/\text{CeO}_2$ nanocomposite exhibits greater photocatalytic activity than the previously obtained $h\text{-YbFeO}_3/o\text{-YbFeO}_3$, pure $o\text{-YbFeO}_3$, and pure CeO_2 .

4. Conclusions

As a result of the work, new I-type heterojunction nanocomposites were successfully developed based on various structural forms of ytterbium orthoferrite and cerium dioxide, which were obtained using the method of solution combustion and heat treatment. A detailed analysis of the composition and structure of $o\text{-YbFeO}_3/h\text{-YbFeO}_3/\text{CeO}_2$ nanocomposites made it possible to determine the features of the formation of this polycrystalline system and the mutual influence of the components on the growth and transformation of the corresponding nanocrystals. The study of the morphological features of nanocomposites and their specific surface area established a positive effect of the foamy microstructure and developed surface on the photocatalytic activity of the samples. The formation of I-type heterojunction had a positive effect on the resulting efficiency of photocatalysts in the Fenton-like process of methyl violet degradation, and the presence of an optimum cerium dioxide content of 5% indicated a complex mutual influence of the components associated with covering active sites on the photocatalyst, shielding the light absorption, decreasing the surface area and activity, increasing the charge recombination. The nanocomposite photocatalysts developed as a result of this work may be of interest for potential use in photo-Fenton-like processes of oxidation of organic pollutants and other advanced oxidation processes.

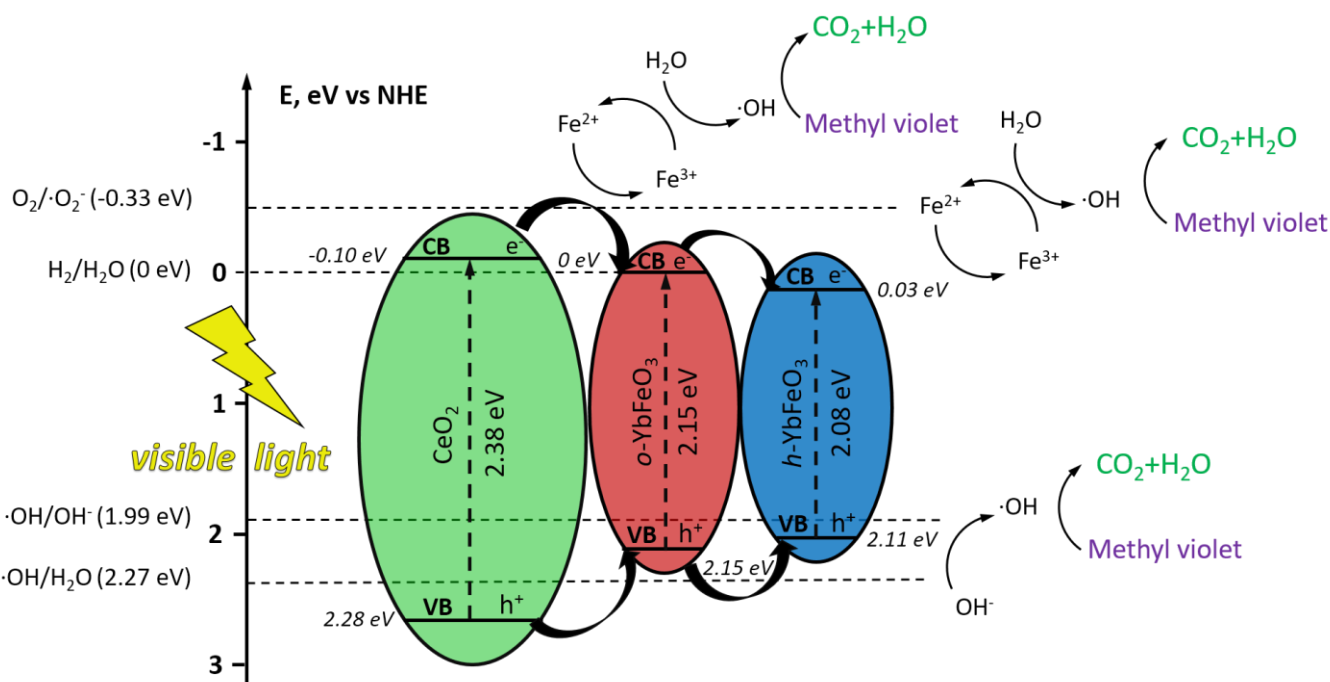


Fig. 10 Schematic mechanism of Fenton-like photodegradation of methyl violet in the presence of heterojunction nanocomposite $o\text{-YbFeO}_3/h\text{-YbFeO}_3/\text{CeO}_2$

Acknowledgments

This work is supported by the Grant of President of the Russian Federation MK-795.2021.1.3. The XRD, SEM, and EDS studies were performed on the equipment of the Engineering Center of Saint Petersburg State Institute of Technology.

References

- Matafonova G, Batoev V. Recent advances in application of UV light-emitting diodes for degrading organic pollutants in water through advanced oxidation processes: A review. *Water Res.* 2018;132:177–189. doi:[10.1016/j.watres.2017.12.079](https://doi.org/10.1016/j.watres.2017.12.079)
- Skvortsova LN, Bolgaru KA, Sherstoboeva MV, Dychko KA. Degradation of diclofenac in aqueous solutions under conditions of combined homogeneous and heterogeneous photocatalysis. *Russ J Phys Chem A.* 2020;94:1248–1253. doi:[10.1134/S0036024420060242](https://doi.org/10.1134/S0036024420060242)
- Makhotkina OA, Preis SV, Parkhomchuk EV. Water delignification by advanced oxidation processes: Homogeneous and heterogeneous Fenton and H₂O₂ photo-assisted reactions. *Appl Catal B Environ.* 2008;84:821–826. doi:[10.1016/j.apcatb.2008.06.015](https://doi.org/10.1016/j.apcatb.2008.06.015)
- Hosokawa S, Jeon HJ, Inoue M. Thermal stabilities of hexagonal and orthorhombic YbFeO₃ synthesized by solvothermal method and their catalytic activities for methane combustion. *Res Chem Intermed.* 2011;37:291–296. doi:[10.1007/s11164-011-0251-9](https://doi.org/10.1007/s11164-011-0251-9)
- Cao S, Sinha K, Zhang X, Zhang X, Wang X, Yin Y. Electronic structure and direct observation of ferrimagnetism in multiferroic hexagonal YbFeO₃. *Phys Rev B.* 2017;95. doi:[10.1103/PhysRevB.95.224428](https://doi.org/10.1103/PhysRevB.95.224428)
- Albadi Y, Sirotkin AA, Semenov VG, Abiev RS, Popkov VI. Synthesis of superparamagnetic GdFeO₃ nanoparticles using a free impinging-jets microreactor. *Russ Chem Bull.* 2020;69:1290–1295. doi:[10.1007/s11172-020-2900-x](https://doi.org/10.1007/s11172-020-2900-x)
- Sklyarova A, Popkov VI, Pleshakov IV, Matveev VV, Štěpánková H, Chlan V. Peculiarities of ⁵⁷Fe NMR Spectrum in micro- and nanocrystalline europium orthoferrites. *Appl Magn Reson.* 2020. doi:[10.1007/s00723-020-01224-y](https://doi.org/10.1007/s00723-020-01224-y)
- Shen T, Hu C, Yang WL, Liu HC, Wei XL. Theoretical investigation of magnetic, electronic and optical properties of orthorhombic YFeO₃: A first-principle study. *Mater Sci Semicond Process.* 2015;34:114–120. doi:[10.1016/j.mssp.2015.02.015](https://doi.org/10.1016/j.mssp.2015.02.015)
- Makoed II, Liedienov NA, Pashchenko AV, Levchenko GG, Tatarchuk DD, Didenko YV. Influence of rare-earth doping on the structural and dielectric properties of orthoferrite La_{0.5}R_{0.5}FeO₃ ceramics synthesized under high pressure. *J Alloys Compd.* 2020;842:155859. doi:[10.1016/j.jallcom.2020.155859](https://doi.org/10.1016/j.jallcom.2020.155859)
- Downie LJ, Goff RJ, Kockelmann W, Forder SD, Parker JE, Morrison FD. Structural, magnetic and electrical properties of the hexagonal ferrites MFeO₃ (M=Y, Yb, In). *J Solid State Chem.* 2012;190:52–60. doi:[10.1016/j.jssc.2012.02.004](https://doi.org/10.1016/j.jssc.2012.02.004)
- Polat O, Coskun M, Coskun FM, Zlamal J, Kurt BZ, Durmus Z. Co doped YbFeO₃: exploring the electrical properties via tuning the doping level. *Ionics.* 2019;25:4013–4029. doi:[10.1007/s11581-019-02934-5](https://doi.org/10.1007/s11581-019-02934-5)
- Dhinesh Kumar R, Thangappan R, Jayavel R. Synthesis and characterization of LaFeO₃/TiO₂ nanocomposites for visible light photocatalytic activity. *J Phys Chem Solids.* 2017;101:25–33. doi:[10.1016/j.jpcs.2016.10.005](https://doi.org/10.1016/j.jpcs.2016.10.005)
- Martinson KD, Kondrashkova IS, Omarov SO, Sladkovskiy DA, Kiselev AS, Kiseleva TY. Magnetically recoverable catalyst based on porous nanocrystalline HoFeO₃ for processes of n-hexane conversion. *Adv Powder Technol.* 2020;31:402–408. doi:[10.1016/j.apt.2019.10.033](https://doi.org/10.1016/j.apt.2019.10.033)
- Baeissa ES. Environmental remediation of aqueous methyl orange dye solution via photocatalytic oxidation using Ag-GdFeO₃ nanoparticles. *J Alloys Compd.* 2016;678:267–272. doi:[10.1016/j.jallcom.2016.04.007](https://doi.org/10.1016/j.jallcom.2016.04.007)
- Liu J, He F, Chen L, Qin X, Zhao N, Huang Y. Novel hexagonal YFeO₃/α-Fe₂O₃ heterojunction composite nanowires with enhanced visible light photocatalytic activity. *Mater Lett.* 2016;165:263–266. doi:[10.1016/j.matlet.2015.12.008](https://doi.org/10.1016/j.matlet.2015.12.008)
- Yang Z, Wu H, Liao J, Li W, Song Z, Yang Y. Infrared to visible upconversion luminescence in Er³⁺/Yb³⁺ co-doped CeO₂ inverse opal. *Mater Sci Eng B.* 2013;178:977–981. doi:[10.1016/j.mseb.2013.06.007](https://doi.org/10.1016/j.mseb.2013.06.007)
- Shao Z, Meng X, Lai H, Zhang D, Pu X, Su C. Coralline-like Ni₂P decorated novel tetrapod-bundle Cd_{0.9}Zn_{0.1}S ZB/WZ homojunctions for highly efficient visible-light photocatalytic hydrogen evolution. *Chinese J Catal.* 2021;42:439–449. doi:[10.1016/S1872-2067\(20\)63597-5](https://doi.org/10.1016/S1872-2067(20)63597-5)
- Hosokawa S, Matsumoto S, Tada R, Shibano T, Tanaka T. Development of Mn-modified hexagonal YbFeO₃ catalyst for reducing the use of precious metal resources. *J Japan Soc Powder Powder Metall.* 2017;64:583–588. doi:[10.2497/jjspm.64.583](https://doi.org/10.2497/jjspm.64.583)
- Tang P, Yu L, Min J, Yang J, Chen H. Preparation of nanocrystalline YbFeO₃ by sol-gel method and its visible-light photocatalytic activities. *Ferroelectrics.* 2017;521:71–76. doi:[10.1080/00150193.2017.1390962](https://doi.org/10.1080/00150193.2017.1390962)
- Jia LX, Zhu JY, Lin TT, Jiang Z, Tang CW, Tang PS. Preparation of YbFeO₃ by microwave assisted method and its visible-light photocatalytic activity. *Adv Mater Res.* 2013;699:708–711. doi:[10.4028/www.scientific.net/AMR.699.708](https://doi.org/10.4028/www.scientific.net/AMR.699.708)
- Kondrashkova IS, Martinson KD, Zakharova NV, Popkov VI. Synthesis of Nanocrystalline HoFeO₃ Photocatalyst via Heat Treatment of Products of Glycine-Nitrate Combustion. *Russ J Gen Chem.* 2018;88:2465–2471. doi:[10.1134/S1070363218120022](https://doi.org/10.1134/S1070363218120022)
- Petschnig LL, Fuhrmann G, Schildhammer D, Tribus M, Schottenberger H, Huppertz H. Solution combustion synthesis of CeFeO₃ under ambient atmosphere. *Ceram Int.* 2016;42:4262–4267. doi:[10.1016/j.ceramint.2015.11.102](https://doi.org/10.1016/j.ceramint.2015.11.102)
- Tikhanova SM, Lebedev LA, Martinson KD, Chebanenko MI, Buryanenko IV, Semenov VG. The synthesis of novel heterojunction h-YbFeO₃/o-YbFeO₃ photocatalyst with enhanced Fenton-like activity under visible-light. *New J Chem. Royal Society of Chemistry.* 2021;45:1541–1550. doi:[10.1039/d0nj04895j](https://doi.org/10.1039/d0nj04895j)
- Popkov VI, Almjasheva OV, Nevedomskiy VN, Sokolov VV, Gusarov VV. Crystallization behavior and morphological features of YFeO₃ nanocrystallites obtained by glycine-nitrate combustion. *Nanosyst Physics, Chem Math.* 2015;6:866–874. doi:[10.17586/2220-8054-2015-6-6-866-874](https://doi.org/10.17586/2220-8054-2015-6-6-866-874)
- Popkov VI, Almjasheva OV, Nevedomskiy VN, Panchuk VV, Semenov VG, Gusarov VV. Effect of spatial constraints on the phase evolution of YFeO₃-based nanopowders under heat treatment of glycine-nitrate combustion products. *Ceram Int.* 2018;44:20906–20912. doi:[10.1016/j.ceramint.2018.08.097](https://doi.org/10.1016/j.ceramint.2018.08.097)
- Kusmieriek E. A CeO₂ semiconductor as a photocatalytic and photoelectrocatalytic material for the remediation of pollutants in industrial wastewater: A review. *Catalysts.* 2020;10:1–54.
- Fan X, Hao H, Shen X, Chen F, Zhang J. Removal and degradation pathway study of sulfasalazine with Fenton-like reaction. *J Hazard Mater.* 2011;190:493–500. doi:[10.1016/j.jhazmat.2011.03.069](https://doi.org/10.1016/j.jhazmat.2011.03.069)
- Wu S, Lin Y, Yang C, Du C, Teng Q, Ma Y. Enhanced activation of peroxymonosulfate by LaFeO₃ perovskite supported on Al₂O₃ for degradation of organic pollutants. *Chemosphere.* 2019;237:124478. doi:[10.1016/j.chemosphere.2019.124478](https://doi.org/10.1016/j.chemosphere.2019.124478)
- Saeed K, Khan I, Gul T, Sadiq M. Efficient photodegradation of methyl violet dye using TiO₂/Pt and TiO₂/Pd photocatalysts. *Appl Water Sci.* 2017;7:3841–3848. doi:[10.1007/s13201-017-0535-3](https://doi.org/10.1007/s13201-017-0535-3)
- Mazarji M, Esmaili H, Bidhendi GN, Mahmoodi NM, Minkina T, Sushkova S. Green synthesis of reduced graphene oxide-CoFe₂O₄ nanocomposite as a highly efficient visible-light-driven catalyst in photocatalysis and photo Fenton-like reaction. *Mater Sci Eng B.* 2021;270:115223. doi:[10.1016/j.mseb.2021.115223](https://doi.org/10.1016/j.mseb.2021.115223)